Solar Phys **(2017) 292:6**
DOI 10.1007/s11207-016-1031-x

Mass-Loss Evolution in the EUV Low Corona from SDO/AIA Data

Fernando M. López[1] · M. Hebe Cremades[2] · Federico A. Nuevo[3] · Laura A. Balmaceda[1,4,5] · Alberto M. Vásquez[3,6]

Received: 8 June 2016 / Accepted: 20 November 2016

Abstract We carry out an analysis of the mass that is evacuated from three coronal dimming regions observed by the *Atmospheric Imaging Assembly* (AIA) on board the *Solar Dynamics Observatory*. The three events are unambiguously identified with white-light coronal mass ejections (CMEs) that are associated in turn with surface activity of diverse nature: an impulsive (M-class) flare, a weak (B-class) flare, and a filament eruption without a flare. The use of three AIA coronal passbands allows applying a differential emission measure technique to define the dimming regions and identify their evacuated mass through the analysis of the electronic density depletion associated with the eruptions. The temporal evolution of the mass loss from the three dimmings can be approximated by an exponential equation followed by a linear fit. We determine the mass of the associated CMEs from COR2 data. The results show that the evacuated masses from the low corona represent a considerable

✉ F.M. López
flopez@icate-conicet.gob.ar

M. Hebe Cremades
hebe.cremades@frm.utn.edu.ar

F.A. Nuevo
federico@iafe.uba.ar

L.A. Balmaceda
lbalmace@gmu.edu

A.M. Vásquez
albert@iafe.uba.ar

1 Instituto de Ciencias Astronómicas, de la Tierra y del Espacio (ICATE), CONICET, San Juan, Argentina

2 Facultad Regional Mendoza—Universidad Tecnológica Nacional, CEDS, CONICET, Mendoza, Argentina

3 Instituto de Astronomía y Física del Espacio (IAFE), CONICET-UBA, Buenos Aires, Argentina

4 Instituto Nacional de Pesquisas Espaciais (INPE), São José dos Campos, Brazil

5 Present address: George Mason University, Fairfax, VA, USA

6 Departamento de Ciencia y Tecnología, Ingeniería Ambiental, Universidad Nacional de Tres de Febrero (UNTREF), Buenos Aires, Argentina

Published online: 08 December 2016

amount of the CME mass. We also find that plasma is still being evacuated from the low corona at the time when the CMEs reach the COR2 field of view. The temporal evolution of the angular width of the CMEs, of the dimming regions in the low corona, and of the flux registered by GOES in soft X-rays are all in close relation with the behavior of mass evacuation from the low corona. We discuss the implications of our findings toward a better understanding of the temporal evolution of several parameters associated with the analyzed dimmings and CMEs.

Keywords Coronal mass ejections · Low coronal signatures · Corona, active · Flares

1. Introduction

Coronal mass ejections (CMEs) are one of the most energetic events generated by the Sun. They transport millions of tons of plasma from the corona into interplanetary space, where they can generate geomagnetic storms on Earth that affect human activities. This is the main reason for which the CME phenomenon has been actively investigated during the past four decades.

The first studies of CMEs showed that CMEs are generally associated with filament eruptions and flares (Munro *et al.*, 1979). However, the origin and nature of the bulk of the CME mass was unclear. The use of *Skylab* coronagraph data allowed Hildner *et al.* (1975) to speculate that the leading edge of mass ejections is mainly composed of material from the lower corona. The analysis of the low-corona observations obtained with a soft X-ray telescope onboard *Skylab* made possible the discovery of intensity depletions at the location of expanding arcs for an event observed on the solar limb (Rust and Hildner, 1976). Later, *Yohkoh* soft X-ray images allowed the observation of intensity depletions associated with halo CMEs for events near solar center (Hudson *et al.*, 1998; Sterling and Hudson, 1997). Similar depletions of intensity were detected in EUV coronal wavelengths (Thompson *et al.*, 1998; Zarro *et al.*, 1999) using data from the *Extreme-ultraviolet Imaging Telescope* (EIT: Delaboudinière *et al.*, 1995). These depletions were similar in appearance to coronal holes, which is why they were referred to as "transient coronal holes" (Zhukov and Auchère, 2004). Further studies confirmed the spatial and temporal association of the onset of CMEs with these transient coronal holes (*e.g.*, Harrison *et al.*, 2003), today known as coronal dimmings.

Using EUV spectroscopic observations from the *Coronal Diagnostic Spectrometer* (CDS: Harrison *et al.*, 1995), Harrison and Lyons (2000) and Harrison *et al.* (2003) determined the mass loss from dimmings observed on the solar limb. The authors found that the mass loss in the dimming regions was on the same order of magnitude as the values estimated for the masses of their associated CMEs. In a later study, Aschwanden *et al.* (2009) used data from the *Extreme-Ultraviolet Imager* (EUVI: Wuelser *et al.*, 2004) onboard the *Solar-Terrestrial Relations Observatory* (STEREO) to obtain the mass loss of eight dimming events, most of them observed on the limb. They compared the results with the mass of the corresponding CMEs determined from the STEREO COR2 coronagraphs, and found a good agreement. In a more recent study, using data from the *EUV Imaging Spectrometer* (EIS: Culhane *et al.*, 2007) on board *Hinode*, Tian *et al.* (2012) found that the mass loss from three dimming regions was in the range of 20 % – 60 % of the masses of their associated CMEs.

It is widely accepted that coronal dimming regions are related to depletions of plasma density in areas associated with eruptions. Dimmings are more easily noticeable in the 195 Å and 211 Å wavelengths than, for instance, at lower-temperature wavelengths such

as at 171 Å. The reason probably is that most of the cooler plasma is not ejected during the opening of loops, remaining gravitationally bound (Robbrecht and Wang, 2010).

Most of the space weather forecasts today rely on the fact that an Earthward CME is detected either by the *Large Angle Spectrometric Coronagraph* (LASCO: Brueckner *et al.*, 1995) onboard the *Solar and Heliospheric Observatory* (SOHO), or by the coronagraphs onboard the STEREO spacecraft. Given the imminent conclusion of the SOHO mission, the strong position dependence of the STEREO remote-sensing data, and the loss of one of the STEREO spacecraft (see http://stereo.gsfc.nasa.gov/status.shtml), the determination of CME masses through low-coronal dimming observations would provide important information regarding potentially geoeffective events. This is particularly valuable for front-sided events, given that measurements of CME masses are not accurate when the CME is propagating far from the plane of the sky (POS), according to the Thomson-scattering theory (Billings, 1966).

The dimmings analyzed in this work are associated with eruption of material from the low corona that can be related to CMEs observed in white light. Our study represents the first analysis of the temporal evolution of mass loss in dimming regions, for which we apply a differential emission measure (DEM) technique on images obtained by the *Atmospheric Imaging Assembly* (AIA: Lemen *et al.*, 2012) onboard the *Solar Dynamics Observatory* (SDO). The deduced values are compared with the masses of the associated CMEs, carefully determined from nearly quadrature coronagraphic images. We use "mass loss" and "evacuated mass" indistinctly to refer to the mass difference in a dimming region at a time before and after the eruption.

The applied DEM technique makes use of data taken by three narrowband EUV imagers that are sensitive to a wide range of temperatures, thus mitigating plasma temperature effects. Other processes that can produce a decrease in the intensity registered in a single wavelength band by EUV telescopes include Doppler effects (Mason *et al.*, 2014). However, these mechanisms (both Doppler dimming and passband shift) do not play a significant role in the present analysis, which is based on the narrowband EUV images taken by the AIA instrument.

In the next section we describe the dimming events under study, their associated CMEs, and the data used for the analysis. In Section 3 we provide a description of the DEM technique, followed by the method we use to estimate the EUV mass loss from the low corona. In Section 4 we determine the CME masses from white-light images, while in Section 5 we compare the EUV and white-light results. Section 6 addresses the temporal relationship between mass loss and X-ray flux profiles. Finally, in Section 7 we summarize our results and present the conclusions.

2. Selected Events

We present the analysis of three events characterized by EUV dimming and an associated CME. All eruptions have been observed in the EUV by AIA onboard the SDO. AIA provides nearly simultaneous full-disk images of the solar corona and transition region in multiple wavelengths with unprecedented temporal and spatial resolution. Full-disk AIA images are recorded with a 12-second cadence and a size of 4096^2 pixels, resulting in a spatial resolution of 1.5 arcsec.

The associated CMEs were observed in white light by the COR1 and COR2 coronagraphs, which are part of the *Sun–Earth Connection Coronal and Heliospheric Investigation* (SECCHI: Howard *et al.*, 2008) onboard the STEREO mission. The COR1 coronagraph

observes the white-light corona with a FOV of 1.4 – 4.0 $R_\odot$, with a 5-minute cadence. The COR2 instrument has a FOV of 2.5 – 15 $R_\odot$ and images the white-light corona with a spatial resolution of 30 arcsec.

The events under study took place between May and November 2010, when the positions of the STEREO twin spacecraft formed an angle of $\approx 70°$ to 85° with the Sun–Earth line. To avoid limb events from the Earth's perspective, the location of the eruptions that caused the dimmings were required to take place in the range of $[-50°, 50°]$ heliographic longitude. At the same time, this implies that their associated CMEs propagate at an angle close to the POS for at least one of the STEREO spacecraft.

The first dimming event (Event 1) occurred on 23 May 2010, starting at 16:52 UT as a B1.4 flare with heliographic coordinates N19 W12, according to the XRT Flare Catalog (Watanabe, Masuda, and Segawa, 2012, http://xrt.cfa.harvard.edu/flare_catalog/). This flare was not registered by the *Geostationary Operational Environmental Satellites* (GOES). For this reason, we perform an analysis of the X-ray and EUV data to verify the existence of the flare. The X-ray and EUV data show the presence of a flare at the location the eruption, supporting the report by the XRT Flare Catalog. EUV images of the low corona show a quiescent filament in eruption from these coordinates, far from any active region. The associated CME is observed close to the POS of the COR2-A and COR2-B, arising in the field of view (FOV) of these instruments at 17:39 UT and 17:54 UT, respectively.

The second dimming (Event 2) took place on 7 August 2010. This event started with a GOES M1.0 flare at 17:55 UT. The event occurred in Active Region (AR) NOAA 11093, with GOES flare coordinates N14 E37. This dimming expanded in association with a coronal wave event, while its corresponding CME was observed by SOHO/LASCO and COR2-B as a partial halo CME. It emerged in the FOV of COR2-A at 18:39 UT, where it propagated close to the POS. Mason *et al.* (2014) investigated this event, and although they did not estimate the mass evacuated from the dimming, they concluded that nearly 100 % of the dimming was due to mass loss in the corona based on the analysis of light curves for different wavelengths from AIA images and EVE data.

The third dimming event (Event 3) was observed by AIA on 30 November 2010. It began as a filament eruption starting at around 17:35 UT with heliographic coordinates N13 E32. No solar flare was registered by GOES or the XRT Flare Catalog that might have been associated with this event. For the previous events we approximate the start time and locations of the eruptions by those reported for the associated flares. However, in this case, the start time and the coordinates of the eruption were derived from AIA images. The CME was observed to propagate close to the POS of COR2-A and COR2-B after 19:24 UT and 20:10 UT, respectively.

3. Determination of Evacuated Mass from the Low Corona

3.1. The Parametric DEM Technique

The DEM technique enables determining the density and temperature of the plasma in the low corona by providing the thermal distribution of the plasma contained in a column along the line of sight (LOS) associated with a pixel. We here use the parametric DEM technique developed by Nuevo *et al.* (2015), adapted for the specific case of high temporal and spatial resolution that is required to analyze dimmings. While DEM distributions can be determined through Markov chain Monte Carlo (MCMC) methods (Kashyap and Drake, 1998) or regularized inversion techniques (Hannah and Kontar, 2012), when high-resolution spectra are

used as input data, parametric DEM studies are a useful approach when based on narrow-band images, as in this work. Similar techniques to the one described below have recently been used, for example to study ARs (Aschwanden and Boerner, 2011; Del Zanna, 2013; Plowman, Kankelborg, and Martens, 2013). A validation study of the parametric technique used here, which compares results to MCMC methods, is included in Nuevo *et al.* (2015).

To obtain the DEM maps of the dimming regions from which the mass loss is estimated, we used the AIA coronal passbands centered at 171 Å (Fe IX), 193 Å (Fe XII/Fe XXIV) and 211 Å (Fe XIV). For these three AIA bands the temperature response function peaks at $\approx$0.9, 1.5, and 1.9 MK, respectively, covering the temperature range characteristic of quiet-Sun regions. For each passband, only three images per minute were averaged to obtain one mean image per minute, so as to increase the signal-to-noise (S/N) ratio. This high cadence still ensures that there are no significant changes in the dimming regions. The standard calibration was applied to the AIA images while rebinning them to a size of 1024^2 pixels, to further increase the S/N ratio and to reduce the calculation time of the DEM algorithms. In order to account for changes in the coronal structures that are due to the differential rotation of the Sun, all images were derotated to a pre-event time. A 2×2 mean filter was finally applied to remove high-frequency noise in the images.

The intensity $I_{k,i}$ registered by the instrument AIA in the passband k in a certain pixel i is given by Equation (1), where $\psi_i(T)$ is the DEM distribution for the pixel i and $Q_k(T)$ is the temperature response function (TRF) of the respective band k,

$$I_{k,i} = \int Q_k(T)\psi_i(T)\mathrm{d}T. \tag{1}$$

The TRF for each band is computed based on the CHIANTI atomic database and plasma emissivity model (Dere *et al.*, 1997) and using the instrumental passbands. Knowing the TRF, the challenge consists of finding the DEM for each pixel that accurately predicts the observed intensity in all three bands. The solution is implemented by considering a family of functions $\psi_i = F(\gamma_i, T)$, with parameters γ_i. When using three EUV bands, an appropriate parametric model $F(\gamma, T)$ is a single Gaussian distribution with three free parameters: the centroid T_0, the standard deviation σ_T, and the amplitude A. For each pixel i, the solution is obtained by finding the values of the parameters γ_i that minimize the quadratic difference between (i) the intensity predicted by the DEM Gaussian model given by Equation (1), and (ii) the observed intensity, summed over all three AIA passbands. For a detailed explanation of the method, we refer to the articles by Frazin, Vásquez, and Kamalabadi (2009) and Nuevo *et al.* (2015), where the DEM parametric technique is developed in the context of EUV tomography. A review of the subject has recently been published by Vásquez (2016).

When the DEM is found, we can derive the emission measure (EM) and the temperature averaged along the LOS by taking the zeroth- and first-order moments of the DEM, specifically,

$$\mathrm{EM} = \int \psi_i(T)\mathrm{d}T \tag{2}$$

$$\langle T \rangle = \int \psi_i(T)T/\mathrm{EM}\mathrm{d}T, \tag{3}$$

while EM is the square density averaged along the LOS,

$$\mathrm{EM} = \int_0^L N_e^2(z)\mathrm{d}z, \tag{4}$$

where z is the coordinate along the LOS and L is the length of the plasma column.

3.2. Definition of the Dimming Region

The usual criterion to identify a dimming in EUV images, assumed to be caused by the evacuation of plasma from an eruption region, is to detect an intensity decrease by using a single coronal passband, for example, 171 Å (*e.g.* Alipour, Safari, and Innes, 2012), 195 Å (*e.g.* Attrill and Wills-Davey, 2010; Reinard and Biesecker, 2008), 193 Å (*e.g.* Krista and Reinard, 2013). However, a dimming may exhibit different characteristics depending on the observation wavelength. To avoid an arbitrary selection of the dimming region by considering any particular AIA passband, we used EM maps constructed from a combination of the three passbands. As the EM is proportional to the square of the local density of plasma, it is a better indicator for the identification of the dimming. Instead of using the full image, we first selected a region of interest (ROI) to determine the dimming areas of the events under study. The AIA 211 Å base-difference ROIs for the three events under study are presented in the left panels of Figure 1. In these panels, the dark areas denote the coronal dimmings, while the bright regions correspond to the post-eruptive loops.

The EM was obtained for all pixels in the ROI, both from pre-eruption and post-eruption images. For each pixel, the difference ΔEM between the post-eruption value ($\mathrm{EM}^{\mathrm{pos}}$) and the pre-eruption value ($\mathrm{EM}^{\mathrm{pre}}$) was computed. A pixel i is considered to belong to the dimming region when the following condition is met,

$$\Delta \mathrm{EM}_i = \left(\mathrm{EM}_i^{\mathrm{pos}} - \mathrm{EM}_i^{\mathrm{pre}}\right) \leq \delta, \tag{5}$$

where δ is the median value of ΔEM for all pixels i that meet $\Delta \mathrm{EM}_i \leq 0$.

The right column in Figure 1 shows color-coded maps of evacuated mass from the low corona ΔM_i (computed through Equation (11) explained below) for all pixels i that fulfill the condition in Equation (5). The deepest intensity drops in the difference images of the left column agree with those regions where the evacuated mass is higher in the right-column color maps, as we ascertain in the following section.

One of the main difficulties in determining the evacuated mass due to the bright post-eruptive loops that appear after the eruption of a CME and cover part of the dimming region. These bright loops contribute significantly to the emission detected in the coronal passbands of AIA, resulting in an increase in density obtained by the DEM analysis. Furthermore, these regions of bright post-eruptive loops, which cover a significant area of the eruption site and are part of the eruptive process, are probably a significant source of mass evacuation. To overcome this problem, we opted to replace the values in the pixels that belong to the post-eruptive loops by a more representative value, determined as follows. We first considered a box that encloses the post-eruptive loops (red box in Figure 1). In the EM base-difference maps, we then selected all pixels i for which $\Delta \mathrm{EM}_i \geq \mu + \sigma$, where μ and σ are the mean and the standard deviation of ΔEM, respectively, for all pixels inside the red box.

After the pixels containing post-eruptive loops were determined, we considered that each of these pixels contributes with a loss of mass equal to the mean value given by the pixels inside the box that fulfill the condition given by Equation (5). Given that it is expected that a large –or even the largest– fraction of the erupted plasma arises from the locations below the post-eruptive loops, by assigning this mean value of evacuated mass, we most likely underestimate the contribution of mass loss from these areas. For a consistency check, the post-eruptive loops in the base-difference images on the left column of Figure 1 can be compared with the uniform color regions at the locations of the loops in the color maps (right column). This is because all pixels containing post-eruptive loops are assigned the same mass-loss value, as stated above.

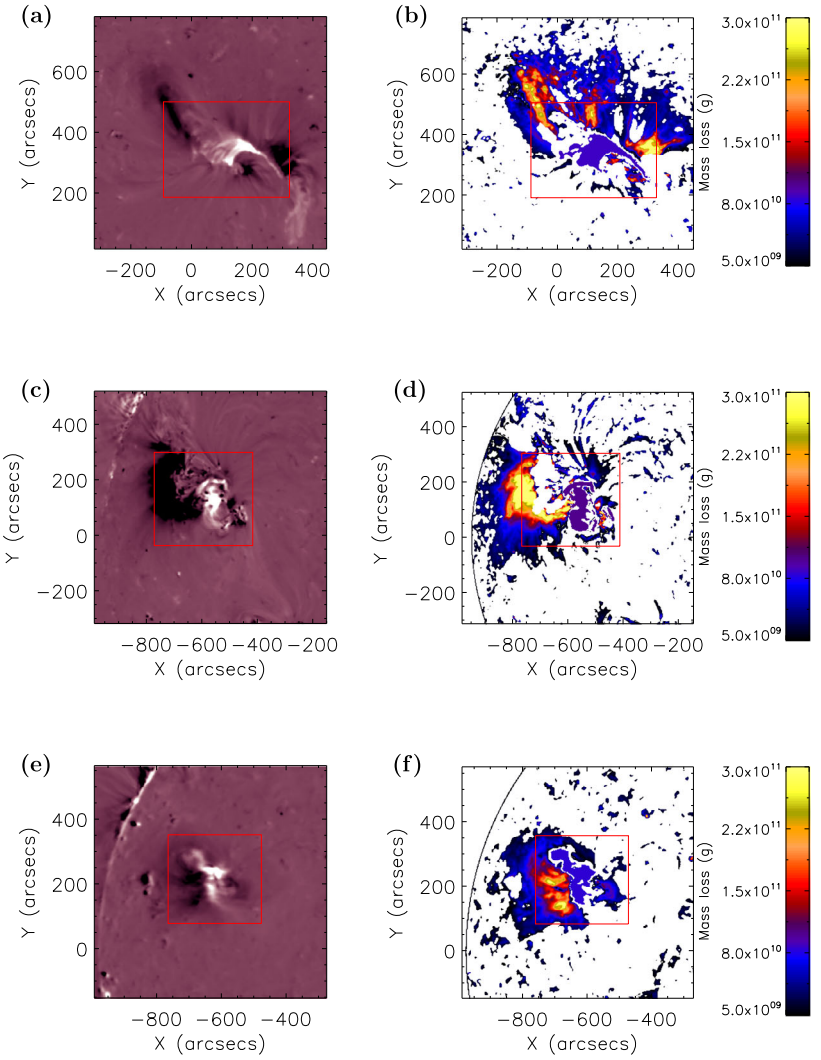

Figure 1 ROI for the events under study. The upper row corresponds to the 23 May 2010 event at 19:00 UT, the middle row to the 7 August 2010 event at 21:00 UT, and the lower row to the 30 November 2010 event at 20:00 UT. Left column: 211 Å base-difference AIA images showing dimmings (dark areas) and post-eruptive loops (bright features). Right column: maps of evacuated mass. The color code indicates mass loss in grams. The coordinates in all plots are given in heliocentric-Cartesian coordinates.

3.3. Estimation of the Evacuated Mass

Under the isothermal hydrostatic equilibrium assumption, the density of the coronal plasma in the dimming region is radially stratified (Aschwanden, 2004),

$$N_e(z) = N_{e0} \exp\left[-\frac{z/\lambda_p}{(z/\mathrm{R}_\odot + 1)}\right]. \quad (6)$$

The pressure scale height is given by

$$\lambda_p = \frac{2k_B T_e}{\mu m_H g_\odot}, \tag{7}$$

where T_e is the electron temperature, k_B the Boltzmann constant, μ the mean molecular weight of the hydrogen ion, m_H the hydrogen mass, and $g_\odot$ the gravitational acceleration at the solar surface. We estimate the pressure scale height using the average temperature obtained from the DEM analysis, *i.e.* $T_e = \langle T \rangle$. From Equation (7), the average pressure scale height $\langle \lambda_p \rangle$ obtained for the ROI pixels of the three events ranges between $\approx$75 Mm to 90 Mm.

The basal electron density N_{e0} can be obtained by inserting Equation (6) into Equation (4)

$$\mathrm{EM} = \int_0^L N_e^2(z)\mathrm{d}z = N_{e0}^2 \frac{\lambda_p}{2} I\left(\frac{\lambda_p}{2\mathrm{R}_\odot}\right), \tag{8}$$

where the length of the plasma column is set to $L = 5\lambda_p$ in order to integrate through the bulk of the mass of the eruption region, and we define the integral quantity

$$I(\alpha) \equiv \int_0^{2L/\lambda_p} \exp\left(-\frac{x}{\alpha x + 1}\right)\mathrm{d}x. \tag{9}$$

The mass M_i along the column of plasma corresponding to any given pixel i can then be estimated as

$$M_i = \mu m_H A_s \int_0^L N_{e,i}(z)\mathrm{d}z = \mu m_H A_s \lambda_{p,i} N_{e0,i} I\left(\frac{\lambda_{p,i}}{\mathrm{R}_\odot}\right), \tag{10}$$

where $A_s = \Omega_p \mathrm{d}_s^2$ is the area of the patch on the Sun that is imaged by each pixel in the detector, with Ω_p being the solid angle subtended by the area of the pixel (A_p) with respect to the effective focal length (f) of the telescope (*i.e.* $\Omega_p = A_p/f^2$), and d_s is the distance of the patch to the telescope. We note that Ω_p is a known intrinsic quantity of the telescope, while d_s is known from the EUV image header. Finally, N_{e0} can be obtained from Equation (8).

To determine the mass loss associated with a pixel i, the difference between the masses for the pre-eruption M_i^{pre} and post-eruption M_i^{pos} images was computed,

$$\Delta M_i = M_i^{\mathrm{pre}} - M_i^{\mathrm{pos}}. \tag{11}$$

The total evacuated mass, ΔM, was computed as the sum of the mass loss from all the pixels of the dimming (fulfilling the condition given by Equation (5)), plus the mass loss associated with the area covered by the post-eruptive loops. The contribution of this last term to the total evacuated mass represents 8 % for Event 1, 7 % for Event 2, and 11 % for Event 3. These values are obtained at the times of the images displayed in Figure 1, when the post-eruptive loops are fully developed. This contribution is insensitive to the size of the red box that was defined such as to enclose the bright post-eruptive loops.

For each event, the total evacuated mass ΔM was computed for a time series of images covering the evolution of the event. The resulting temporal behavior of the evacuated mass for the three analyzed events is shown in Figure 2. The mass-loss values determined every 10 minutes are represented by asterisks joined by lines. The red lines represent a fit to the values, comprised of two different functions. The first section represents the high rate of plasma evacuation in the initial stages, for which we use this Equation (12):

$$\Delta M(t) = A\left(1 - e^{-Bt}\right). \tag{12}$$

This equation was proposed by Colaninno and Vourlidas (2009, their Equation 11) to fit the white-light mass evolution of eight CMEs. We used a nonlinear least-squares fit, with initial

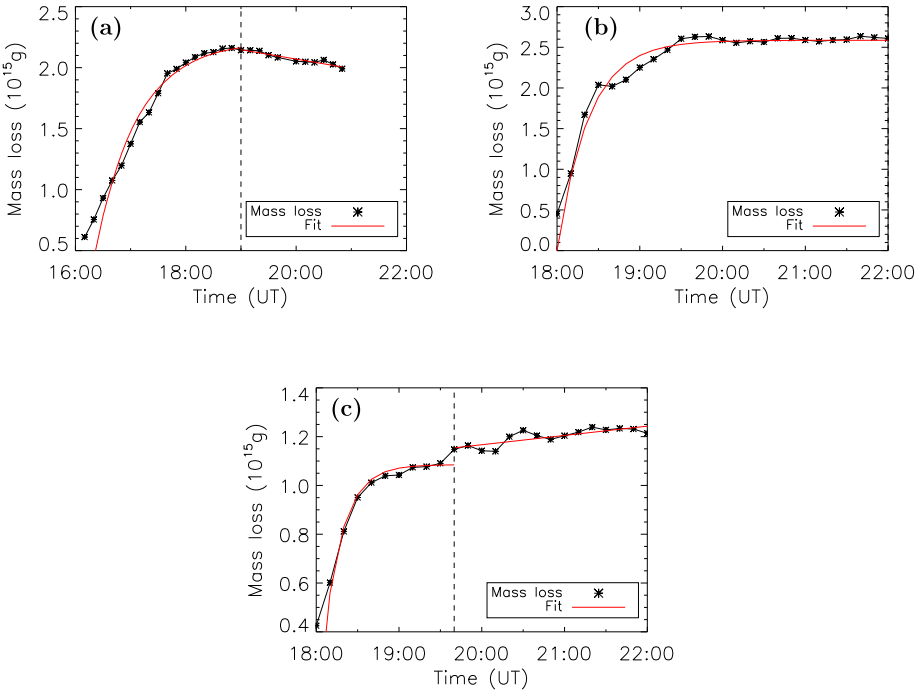

Figure 2 Temporal evolution of the mass loss from the low corona (asterisks joined with a line) for the events under study: 23 May 2010 (a), 7 August 2010 (b) and 30 November 2010 (c). Red solid lines represent the fit to the estimated mass values for each event, while the vertical dashed lines indicate the change in fitting function (see text).

guesses $[A, B] = [\Delta M_{\rm top}, \frac{3}{t_c}]$, where $\Delta M_{\rm top}$ is the maximum value of the mass loss and t_c is the time when the mass loss reaches 63 % of the $\Delta M_{\rm top}$ value.

The second function of the fit in Figure 2 is provided by a linear model, which represents the gradual recovery of the mass loss, as in Figure 2a, or a phase of slower evacuation of plasma, as in the case of Figure 2c. For Event 2 in Figure 2b, Equation (12) was enough to describe the complete evolution during the analyzed time interval because the mass loss approaches a constant value. The vertical dashed line in Figures 2a and c indicates the change in fitting function.

4. CME Mass Determination

It is known that the intensity registered by white-light coronagraphs is due to Thomson scattering of photospheric light by free electrons in the solar corona, with this intensity being the result of the individual contribution by all scattering elements along the LOS. This process is more efficient when the scattering electrons are located closer to the Thomson surface (*e.g.* Vourlidas and Howard, 2006). This surface is a sphere with a diameter equal to the Sun–observer distance. For COR2 white-light coronagraphs with a FOV $\leq$ 15 solar radii, the POS and the sphere can be considered as coincident. The emission decreases with the distance to this plane, producing an underestimation of the number of electrons of a CME when it is in fact propagating with a certain angle respect to the POS.

Table 1 Various parameters obtained for Events 1 – 3. Column 1 refers to the event identification number, and columns 2 – 4 correspond to parameters obtained by the forward-modeling approximation. Columns 5 and 6 show the CME acceleration and speed at the height of the last measurement, obtained from a second-order fit. Columns 7 and 8 are the masses deduced from the white-light and EUV data, respectively, while column 9 shows the consequent ratio between them.

#	Prop. dir. [lat., long.]	ω_A (deg.)	ω_B (deg.)	Acc. ($m\,s^{-2}$)	Speed ($km\,s^{-1}$)	M_{CME} (10^{15} g)	M_{EUV} (10^{15} g)	Ratio (%)
(1)	(2)	(3)	(4)	(5)	(6)	(7)	(8)	(9)
1	[N08,015]	34	5	10.8	445.68	3.21	2.16	67.2
2	[N05,317]	32	62	−8.2	761.97	7.06	2.63	37.2
3	[N03,328]	27	39	17.4	600.80	2.11	1.23	58.3

To determine the true propagation direction of the CMEs, we applied the forward-modeling method developed by Thernisien, Vourlidas, and Howard (2009) to simulate the CME simultaneously from three points of view to minimize errors in the fit. The three views are given by COR2-A, COR2-B, and LASCO C2 images, whose unrelated background and structures were removed by subtracting a suitable pre-event image. Table 1 shows some of the parameters obtained after applying this forward-modeling approximation to the three events. Column 1 indicates the event number, while column 2 shows the Stonyhurst coordinates for the propagation direction of the CMEs with respect to the Sun–Earth line. The angle subtended by the propagation direction of the CMEs wih respect to the POS of COR2-A and COR2-B is given in columns 3 and 4 by ω_A and ω_B, respectively. To measure the CME mass of the three events, we only used coronagraphic data of the spacecraft where the direction of propagation is closer to the respective POS, *i.e.* depending on whether the lowest value is given by ω_A or ω_B.

After determining the direction of propagation of the CMEs, the total-brightness intensity images were converted into mass images by the Thomson scattering equations (Billings, 1966), following the method described in Vourlidas *et al.* (2010). Here we considered that all electrons lie on a plane at the corresponding angle ω relative to the POS, either ω_A or ω_B. The total mass of the CMEs was obtained by adding the contribution of the mass contained in each pixel that belongs to the CME. The boundary of the CME was then manually selected in the mass images, using the freehand ROI method. In this way, all the pixels enclosed in the ROI contribute to the CME mass. The CME mass values M_{CME} presented in column 7 of Table 1 are deduced from the last available image of the corresponding CME before it leaves the FOV of COR2.

To verify the validity of the results of our mass measurements from a single point of view, we applied the method presented in Colaninno and Vourlidas (2009), which takes advantage of the two STEREO points of view to estimate the true CME masses. Using this approach, we calculated the true mass of a CME M_T with the equation $M_T = (M_A - M_B)/(f_m(\omega_A) - f_m(\omega_B))$, where M_A and M_B are the masses determined from COR2-A and COR2-B, respectively, considering the POS assumption ($\omega = 0$). The angles ω_A and ω_B represent the angular separation between the CME propagation direction and the respective POS of COR2-A and COR2-B. The function $f_m(\omega)$ is the ratio of the brightness of an electron at an angle ω relative to its brightness on the POS: $f_m(\omega) = B_e(\omega)/B_e(\omega = 0)$.

The resulting masses obtained by applying the method by Colaninno and Vourlidas (2009) are in good agreement with those found from single-spacecraft data. Differences in the masses obtained by the two methods are on the order of ~ 6 % for Events 1 and 3.

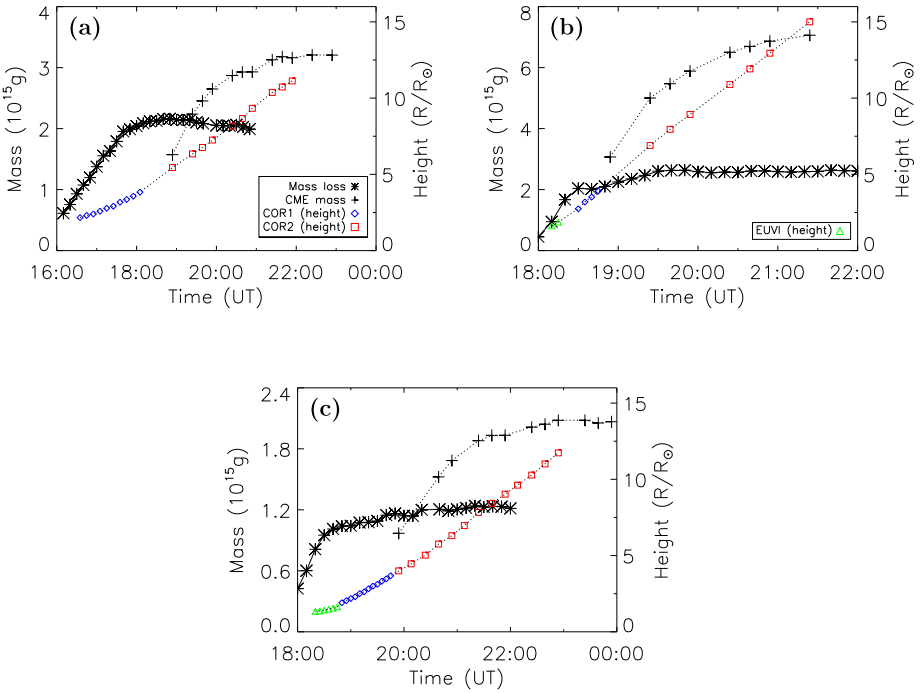

Figure 3 Temporal evolution of EUV mass loss (asterisks) and white-light CME mass (plus signs) for the events under study: 23 May 2010 (a), 7 August 2010 (b) and 30 November 2010 (c). The deprojected height–time points corresponding to the CME leading edge are also shown, with green triangles representing the EUVI measurements, blue diamonds those of COR1, and red squares those of COR2.

However, for Event 2, whose CME is a partial halo from COR2-B, the discrepancy is considerably higher. A similar result is also reported by these authors, who did not find a good agreement for the case of a partial halo CME event, indicating a limitation in the accuracy of their method when the CME travels far from the POS of at least one of the spacecraft. Because of this shortcoming for Event 2 and the small differences for Events 1 and 3, we prefer to list in Table 1 only the CME mass deduced from single-spacecraft data.

5. Comparison of CME Mass and Mass Loss in the Low Corona

In this section, we present the results that arise from the comparison between (i) the masses determined for the CMEs from white-light coronagraphic observations, and (ii) the evacuated mass from the associated dimming regions from EUV images. Column 8 of Table 1 displays the obtained values of the mass loss in the three dimming regions (M_{EUV}), while column 9 shows the percentage ratio of M_{EUV}/M_{CME} (Ratio).

Figure 3 shows the temporal evolution of the EUV mass loss in comparison with that of the associated CME mass for the three events. Both curves present an initial fast-rise phase followed by a considerably slower variation in time. The evident temporal offset between the mass loss and the CME mass temporal profiles can be attributed to the mass of the CME emerging into the COR2 FOV as the CME propagates outward from behind the occulter.

In addition, Figure 3 displays the deprojected height (*i.e.* corrected by the angle of propagation ω, addressed in the previous section) of the CME leading edge as a function of time, determined from EUVI, COR1, and COR2 observations. For Event 1, it was not possible to clearly identify the CME front in the low corona. However, a second-order profile is shown from the COR1 points. Event 2 exhibits an almost linear profile, even at low coronal heights. The kinematic evolution of Event 3 shows an accelerated profile for the first set of points, while it can be considered linear after ≈ 3 $R_\odot$. For completeness, the acceleration and the speed at the height of the last measurement, obtained from a second-order fit, are shown in columns 5 and 6 of Table 1. From Figure 3, we can also infer that the highest rate of mass evacuation from the dimming regions takes place when the CMEs are traveling through the FOV of EUVI and COR1. The evacuation of plasma continues even when the CME leading edge is at COR2 coronal heights, persisting up to ≈ 5 $R_\odot$ for Event 1 and ≈ 7 $R_\odot$ for Event 2. Event 3 presents mass loss when the CME is beyond 10 $R_\odot$, although at a considerable lower pace. However, it must be noted that the mass supplied from the low corona during the propagation of the three CMEs in the COR2 FOV is small in comparison with the difference between M_{CME} and M_{EUV}. This difference may in part be due to the mass that the CMEs may add during their propagation in the higher lying corona they pass through, as summarized in Section 7.

To investigate the temporal evolution of the CME angular width (AW) from the low corona and up to the reach of COR2 FOV, we have determined the angular span of the CME in EUVI, COR1, and COR2 images. In the left column of Figure 4 we show the results of these measurements determined from EUV and white-light data in comparison with the AW of the dimming regions and the mass loss from the low corona. All AWs have been normalized to the respective maximum values, displayed in the plots as $\max(AW_D)$ and $\max(AW_{CME})$.

The determination of the CME AW was carried out in images provided by STEREO A or B, depending on which spacecraft detected the CME traveling closer to its POS.

We calculated the uncertainties in the CME AW estimation as $\sigma_{AW} = 2(\sigma_m/R_{oc})$ (in radians), where (σ_m) is the error in the measurement of the position of a CME flank, and R_m is the height of the measurement. The considered values of (σ_m) are 0.01 $R_\odot$ for EUVI, 0.04 $R_\odot$ for COR1, and 0.17 $R_\odot$ for COR2 at a height R_m of 1 $R_\odot$ for EUVI and at the border of the occulter for each coronagraph. These values of R_m correspond to the heights at which the measurements of the CME flanks are approximately performed. The errors in the AW of the CMEs are thus estimated to be 1.1° for EUVI, 3.0° for COR1 and 7.8° for COR2.

The AW of the dimming, on the other hand, was determined by considering the dimming as a disk of area A_D and radius $R_D = \sqrt{A_D/\pi}$. The area on the spherical surface of the Sun, covered by a pixel i is determined as $a_{d,i} = A_s/(\cos(\rho_i))$, with ρ being the angle between the normal to the local surface and the direction to the observer, and A_s the same as defined in Section 3.3. The area of the dimming (A_D) was obtained after summing the area on the surface of the Sun contained by all pixels that belong to the dimming $(A_D = \sum a_d)$. The AW of the dimming region (AW_D) is then given by the relation $AW_D = 2\arctan(R_D/1\ R_\odot)$.

The profiles of normalized AW of the dimming regions and of the CMEs in the left column of Figure 4 exhibit a good concordance. In turn, the two AW profiles are also in agreement with the temporal evolution of the mass loss. The AW for both the CME and the dimming increases during the phase of highest plasma evacuation rate. Likewise, both AWs become stable roughly at the time when the mass evacuation ceases. Event 2, which is associated with an M-class flare, presents the maximum change of normalized AW at COR1 heights, from ≈ 0.4 to 1.0, while in the FOV of EUVI it changes from ≈ 0.1 to 0.4. Event 1,

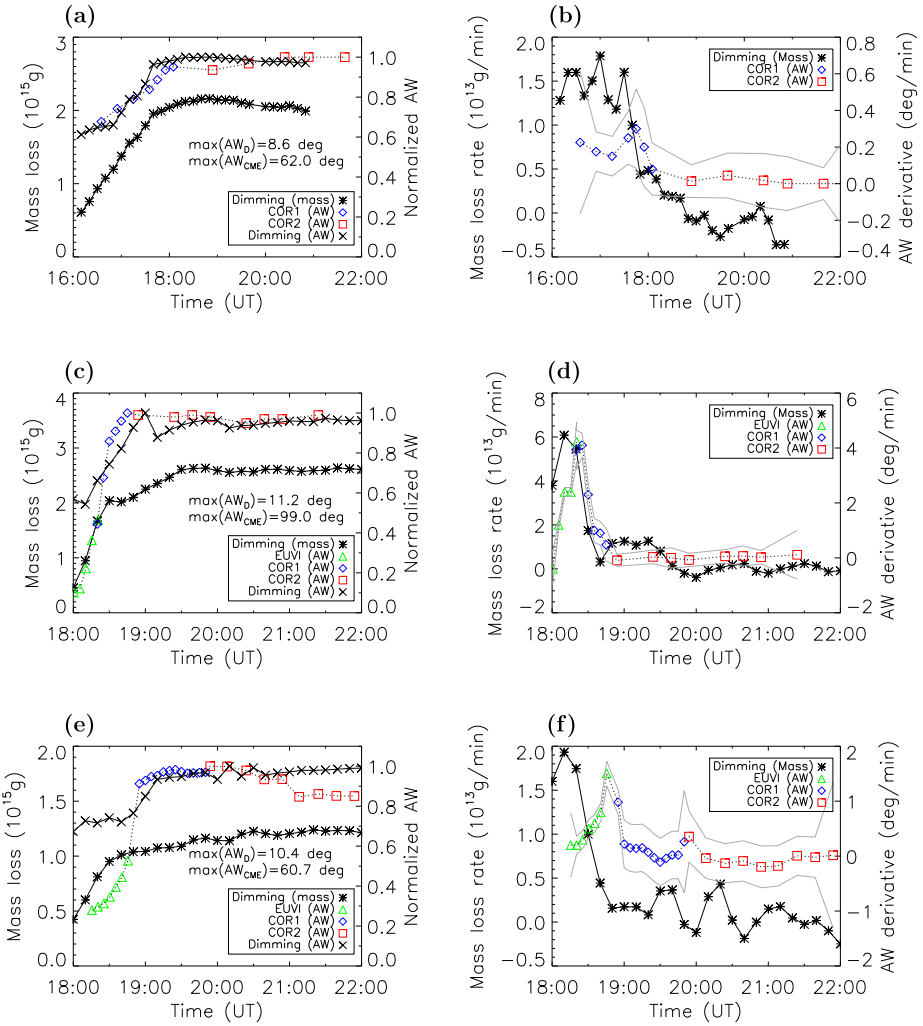

Figure 4 Left column: temporal evolution of the normalized AW of the dimming area defined by the DEM (crosses), of the CME in EUVI (green triangles), COR1 (blue diamonds) and COR2 (red squares), for Event 1 (a), Event 2 (c) and Event 3 (e). The maximum AW values used to normalize the AWs of the dimmings and of the CMEs are shown in the plots as $\max(\mathrm{AW}_D)$ and $\max(\mathrm{AW}_{\mathrm{CME}})$ respectively. The measurements of the AW of the CME in the three instruments are joined by a dotted line. For comparison, the low coronal evacuated mass is also displayed (asterisks). Right column: derivative of the CME AW at the times of the AW measurements using the same symbols as in (a), (c) and (e). The band delimited by the gray continuous lines in figures (b), (d), and (f) shows the uncertainty in the AW derivatives. For comparison, the derivative of the evacuated mass is also displayed (asterisks).

related to a B-class flare, shows a change of $\approx 0.7-1.0$ in COR1. As for Event 3, which could not be associated with any flare, its change in normalized AW is merely from ≈ 0.9 to 1.0 in COR1, while most of its expansion takes place in EUVI, from ≈ 0.3 to at least 0.5. The analysis of these three events suggests a possible relationship between the intensity of the associated flare and the relative expansion of the CME. On the one hand, the more intense the flare, the larger the change of normalized AW at COR1 heights. On the other

hand, the less energetic the flare (Event 3 lacks a flare), the lower the height at which most of the CME expansion takes place. Naturally, this result cannot be generalized and may only apply to this small set of analyzed events.

The right column in Figure 4 shows the derivative of the CME AW together with that of the evacuated mass as a function of time. The AW and mass-loss derivatives are obtained by applying a three-point Lagrangian interpolation. There is a good overall agreement in the general behavior of the derivatives of AW and mass-loss profiles in time and relative amplitude. The largest AW rates match in time with the growth of mass-loss rate for Events 1 and 2, while both rates decrease and become stable simultaneously. For Event 3 there is an initial disagreement in time between the AW and mass-loss derivatives. The highest mass-loss rates occur when the opening of the EUV loops starts to develop, while the peak of the AW derivative takes place when the mass-loss rate has decreased significantly. After this, both profiles decrease slowly, with the AW derivative profile becoming more stable. In correspondence with the interpretation of the plots in the first column of the figure, the highest AW rates are achieved by Event 2. Events 1 and 3 reach lower peak values of AW rate, with the expansion of Event 1 being more sustained over time, most likely because we were not able to perform AW measurements in EUVI for this event.

6. Temporal Evolution of the Evacuated Mass and X-Ray Flux

Two of the analyzed events, namely Events 1 and 2, are associated with X-ray flares, which led us to search for temporal correspondences between the profile of the EUV mass evacuation and that of the respective flares described by the variation of the X-ray flux. Event 3 is not associated with a cataloged flare, and from direct inspection of GOES data, we could not detect any increase in the soft X-ray flux at the time of the eruption. In Figure 5 we plot the EUV mass-loss evolution and the X-ray flux profile registered by GOES (0.1 – 0.8 nm) for Events 1 and 2 (panels a and c). For Event 1, Figure 5a reveals that there is evacuation of mass from the low corona minutes before the X-ray flux increment. This time difference could be either due to plasma flows before the eruption (Vourlidas, Syntelis, and Tsinganos, 2012), or due to the initial launch phase of the CME. For Event 2, the first EUV mass estimation available after the dimming onset matches the beginning of the flare rising phase. It is worth noting that this event is very impulsive, associated with an M-class flare; as opposed to Event 1, which is related to a more slowly rising B-class flare.

Figures 5b and d display for Events 1 and 2 the derivative of the X-ray flux in comparison with that of the mass loss as a function of time. The derivative profiles in Figure 5b exhibit a similar slope after the flare onset and even after the evacuated mass reaches its maximum value. For Event 2 (Figure 5d), a good temporal agreement between the flare peak and the time of highest plasma evacuation rate is observed. Several authors have previously reported a close correspondence between soft X-ray flux and acceleration profiles of CMEs (*e.g.* Zhang *et al.*, 2004; Vourlidas, Syntelis, and Tsinganos, 2012). Since the dimmings studied in this work are associated with the evacuation of plasma, which implies acceleration of material during the eruption, a good concordance between the mass loss and X-ray flux profiles is reasonable to expect.

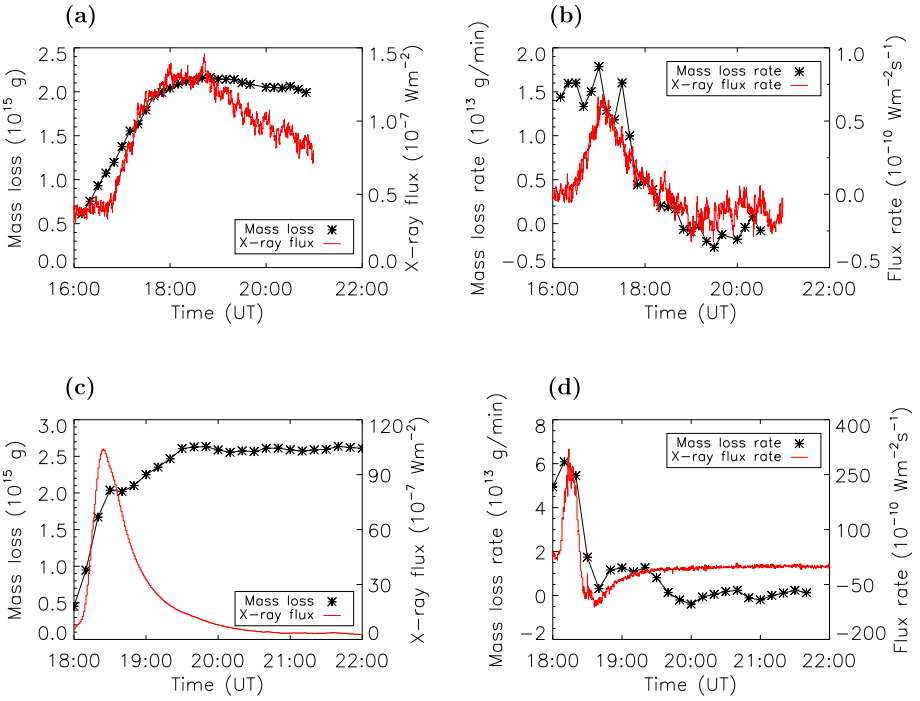

Figure 5 Left column: X-ray flux from GOES measurements (red solid line) and mass loss from the low corona (asterisks) for Events 1 (a) and 2 (c). Right column: derivative of the X-ray flux (flux rate, red solid line) and of the mass loss (mass-loss rate, asterisks).

7. Summary and Conclusions

We reported on the analysis of three coronal dimmings and their associated CMEs, for which we applied separate techniques to estimate both the CME mass and the evacuated mass from the associated EUV dimmings, and analyzed their relation.

The evacuated coronal mass was estimated with a DEM technique applied to the dimming regions using data from three AIA coronal passbands. The mass-loss color maps deduced for each of the dimming regions indicate that the evacuation of plasma is not uniform. Mass loss is highest in some of the periphery regions of the bright post-eruptive loops, with Event 1 exhibiting a double-dimming pattern at the location of the ejected filament footpoints (Thompson *et al.*, 2000).

We determined the mass loss during several hours after the events, whose temporal behavior is different in the three cases. Although a stage of similar high evacuation rate in the low corona is common for the three events, the following phase differs, with one of the events presenting a gradual recovery (Event 1), another showing additional evacuation (Event 3), and the remaining event exhibiting none of them, which could also imply that recovery and evacuation of plasma in the low corona balance each other (Event 2). These three behaviors were described with the aid of an exponential fit followed by a linear one.

Height–time measurements of the leading edge of the CMEs from the low corona and up to the reach of the STEREO coronagraphs indicate that most of the plasma is evacuated from the low corona when the CMEs are traveling through the FOV of EUVI and COR1.

Even when the CMEs are propagating in the FOV of COR2, mass is still being evacuated from the low corona, although at a considerably lower rate.

The temporal evolutions of dimming and CME AWs are in good agreement with each other, and also correspond well with the respective mass-loss profiles. The similarity between the AW and the mass-loss profiles is remarkable, suggesting that these two attributes are closely related. The analysis of the AW behavior in time suggests that most of the expansion takes place at higher altitudes for the events associated with larger flares, at least for the three events we investigated here.

For the two events associated with flares, we examined the correspondence between the soft X-ray flux registered by GOES and the mass-loss profiles. The beginning of mass evacuation precedes the flare rising phase in Event 1, while both concur in Event 2. In addition, there is a good match between the peaks of mass loss and X-ray flux derivatives.

The temporal evolution of the dimming area, the CME AW, and the flare X-ray flux associated with each low-coronal event suggest a close connection to the process of mass evacuation in the EUV low corona.

The mass of the associated white-light CMEs was determined using COR2 total-brightness images. The total mass loss determined from EUV data differs by $\approx 33-63$ % with respect to the white-light CME mass, depending of the event. Still, the evacuated mass from the coronal dimmings represents a considerable amount of the mass of the associated CMEs. Our results using AIA data represent a similar fraction of the CME mass with regard to other reports based on data from other instruments (*e.g.* Harrison *et al.*, 2003; Aschwanden *et al.*, 2009; Tian *et al.*, 2012). At the same time, as opposed to some of these reported results, we find that the low-coronal evacuated mass determined from a DEM analysis is not sufficient to account for all the mass measurable in the white-light associated CMEs. Several aspects play a key role in the accuracy of EUV evacuated mass and white-light mass determination. The evacuated mass in the low corona is certainly underestimated and should be taken as a lower limit because of the reasons we list below.

- Prominences represent the brightest part of CMEs in white-light coronagraphic images, forming the bright core of these events. Their mass measured in EUV is in the range $10^{14}-10^{15}$ g (Gilbert *et al.*, 2006), providing a considerable contribution to the mass of CMEs. This material is assumed to be of chromospheric origin and thus at a lower temperature. Therefore the characteristic temperature of the EUV passbands we analyzed here may not account for the contribution of mass of this cooler material.
- At the same time, prominence material on the disk is seen in absorption in EUV images, decreasing the emission measure obtained at the pre-event time, while bright post-eruptive loops cover a significant area of the eruption site, where most of the evacuation of plasma is assumed to take place.
- In addition, because of the temperature covered by the used AIA passbands, the contribution of hot plasma (≥ 2.5 MK) is not considered in the determination of the mass evacuated from the low corona.

On the other hand, the difference with the mass of the CME estimated from white-light observations can be at least partly explained by the reasons listed below.

- The CME mass is assumed to be composed not only of plasma evacuated from the low corona, but also of mass provided by the cold prominence and by material that is piled up during the CME propagation (Feng *et al.*, 2015).
- The difference between the white-light CME mass and the EUV evacuated mass can also be attributed to the limitations in the methods used to determine the mass from white-light observations. For instance, the strong dependence on the relative position of the observer

with respect to the direction of propagation, and the unknown density distribution within CMEs (Vourlidas *et al.*, 2000), involve significant uncertainties in the CME mass determination.

We are currently performing similar analyses on a larger sample of events. We intend to find associations among parameters related to EUV mass loss and white-light CME mass that may be helpful to deduce CME properties from low coronal data. Furthermore, we aim to gain an understanding of how the error sources affect events with different characteristics.

Acknowledgements FML and FAN are fellows of CONICET. HC and AMV are members of the Carrera del Investigador Científico (CONICET). FML, HC, and LAB appreciate support from project UTN UTI1744. The authors thank the anonymous referee for very constructive comments and suggestions, as well as Marc L. DeRosa and Barbara Thompson for helpful discussions. The authors acknowledge the use of data from the SDO/AIA and STEREO/SECCHI projects. The AIA data used here are courtesy of SDO (NASA) and the AIA consortium. The SECCHI data are courtesy of STEREO and the SECCHI consortium.

Disclosure of Potential Conflicts of Interest The authors declare that they have no conflicts of interest.

References

Alipour, N., Safari, H., Innes, D.E.: 2012, An automatic detection method for extreme-ultraviolet dimmings associated with small-scale eruption. *Astrophys. J.* **746**, 12. DOI. ADS.

Aschwanden, M.J.: 2004, *Physics of the Solar Corona. An Introduction*. ADS.

Aschwanden, M.J., Boerner, P.: 2011, Solar corona loop studies with the atmospheric imaging assembly. I. Cross-sectional temperature structure. *Astrophys. J.* **732**, 81. DOI. ADS.

Aschwanden, M.J., Nitta, N.V., Wuelser, J.-P., Lemen, J.R., Sandman, A., Vourlidas, A., Colaninno, R.C.: 2009, First measurements of the mass of coronal mass ejections from the EUV dimming observed with STEREO EUVI A+B spacecraft. *Astrophys. J.* **706**, 376. DOI. ADS.

Attrill, G.D.R., Wills-Davey, M.J.: 2010, Automatic detection and extraction of coronal dimmings from SDO/AIA data. *Solar Phys.* **262**, 461. DOI. ADS.

Billings, D.E.: 1966, *A Guide to the Solar Corona*. ADS.

Brueckner, G.E., Howard, R.A., Koomen, M.J., Korendyke, C.M., Michels, D.J., Moses, J.D., Socker, D.G., Dere, K.P., Lamy, P.L., Llebaria, A., Bout, M.V., Schwenn, R., Simnett, G.M., Bedford, D.K., Eyles, C.J.: 1995, The Large Angle Spectroscopic Coronagraph (LASCO). *Solar Phys.* **162**, 357. DOI. ADS.

Colaninno, R.C., Vourlidas, A.: 2009, First determination of the true mass of coronal mass ejections: a novel approach to using the two STEREO viewpoints. *Astrophys. J.* **698**, 852. DOI. ADS.

Culhane, J.L., Harra, L.K., James, A.M., Al-Janabi, K., Bradley, L.J., Chaudry, R.A., Rees, K., Tandy, J.A., Thomas, P., Whillock, M.C.R., Winter, B., Doschek, G.A., Korendyke, C.M., Brown, C.M., Myers, S., Mariska, J., Seely, J., Lang, J., Kent, B.J., Shaughnessy, B.M., Young, P.R., Simnett, G.M., Castelli, C.M., Mahmoud, S., Mapson-Menard, H., Probyn, B.J., Thomas, R.J., Davila, J., Dere, K., Windt, D., Shea, J., Hagood, R., Moye, R., Hara, H., Watanabe, T., Matsuzaki, K., Kosugi, T., Hansteen, V., Wikstol, Ø.: 2007, The EUV Imaging Spectrometer for Hinode. *Sol. Phys.* **243**, 19. DOI. ADS.

Del Zanna, G.: 2013, The multi-thermal emission in solar active regions. *Astron. Astrophys.* **558**, A73. DOI. ADS.

Delaboudinière, J.-P., Artzner, G.E., Brunaud, J., Gabriel, A.H., Hochedez, J.F., Millier, F., Song, X.Y., Au, B., Dere, K.P., Howard, R.A., Kreplin, R., Michels, D.J., Moses, J.D., Defise, J.M., Jamar, C., Rochus, P., Chauvineau, J.P., Marioge, J.P., Catura, R.C., Lemen, J.R., Shing, L., Stern, R.A., Gurman, J.B., Neupert, W.M., Maucherat, A., Clette, F., Cugnon, P., van Dessel, E.L.: 1995, EIT: extreme-ultraviolet imaging telescope for the SOHO mission. *Solar Phys.* **162**, 291. DOI. ADS.

Dere, K.P., Landi, E., Mason, H.E., Monsignori Fossi, B.C., Young, P.R.: 1997, CHIANTI – an atomic database for emission lines. *Astron. Astrophys. Suppl.* **125**, 149. DOI. ADS.

Feng, L., Wang, Y., Shen, F., Shen, C., Inhester, B., Lu, L., Gan, W.: 2015, Why does the apparent mass of a coronal mass ejection increase? *Astrophys. J.* **812**, 70. DOI. ADS.

Frazin, R.A., Vásquez, A.M., Kamalabadi, F.: 2009, Quantitative, three-dimensional analysis of the global corona with multi-spacecraft differential emission measure tomography. *Astrophys. J.* **701**, 547. DOI. ADS.

Gilbert, H.R., Falco, L.E., Holzer, T.E., MacQueen, R.M.: 2006, Application of a new technique for deriving prominence mass from SOHO EIT Fe XII (19.5 nm) absorption features. *Astrophys. J.* **641**, 606. DOI. ADS.

Hannah, I.G., Kontar, E.P.: 2012, Differential emission measures from the regularized inversion of Hinode and SDO data. *Astron. Astrophys.* **539**, A146. DOI. ADS.

Harrison, R.A., Lyons, M.: 2000, A spectroscopic study of coronal dimming associated with a coronal mass ejection. *Astron. Astrophys.* **358**, 1097.

Harrison, R.A., Sawyer, E.C., Carter, M.K., Cruise, A.M., Cutler, R.M., Fludra, A., Hayes, R.W., Kent, B.J., Lang, J., Parker, D.J., Payne, J., Pike, C.D., Peskett, S.C., Richards, A.G., Gulhane, J.L., Norman, K., Breeveld, A.A., Breeveld, E.R., Al Janabi, K.F., McCalden, A.J., Parkinson, J.H., Self, D.G., Thomas, P.D., Poland, A.I., Thomas, R.J., Thompson, W.T., Kjeldseth-Moe, O., Brekke, P., Karud, J., Maltby, P., Aschenbach, B., Bräuninger, H., Kühne, M., Hollandt, J., Siegmund, O.H.W., Huber, M.C.E., Gabriel, A.H., Mason, H.E., Bromage, B.J.I.: 1995, The coronal diagnostic spectrometer for the solar and heliospheric observatory. *Solar Phys.* **162**, 233. DOI. ADS.

Harrison, R.A., Bryans, P., Simnett, G.M., Lyons, M.: 2003, Coronal dimming and the coronal mass ejection onset. *Astron. Astrophys.* **400**, 1071. DOI. ADS.

Hildner, E., Gosling, J.T., Hansen, R.T., Bohlin, J.D.: 1975, The sources of material comprising a mass ejection coronal transient. *Solar Phys.* **45**, 363. DOI. ADS.

Howard, R.A., Moses, J.D., Vourlidas, A., Newmark, J.S., Socker, D.G., Plunkett, S.P., Korendyke, C.M., Cook, J.W., Hurley, A., Davila, J.M., Thompson, W.T., St Cyr, O.C., Mentzell, E., Mehalick, K., Lemen, J.R., Wuelser, J.P., Duncan, D.W., Tarbell, T.D., Wolfson, C.J., Moore, A., Harrison, R.A., Waltham, N.R., Lang, J., Davis, C.J., Eyles, C.J., Mapson-Menard, H., Simnett, G.M., Halain, J.P., Defise, J.M., Mazy, E., Rochus, P., Mercier, R., Ravet, M.F., Delmotte, F., Auchere, F., Delaboudiniere, J.P., Bothmer, V., Deutsch, W., Wang, D., Rich, N., Cooper, S., Stephens, V., Maahs, G., Baugh, R., McMullin, D., Carter, T.: 2008, Sun Earth Connection Coronal and Heliospheric Investigation (SECCHI). *Space Sci. Rev.* **136**, 67. DOI. ADS.

Hudson, H.S., Lemen, J.R., St. Cyr, O.C., Sterling, A.C., Webb, D.F.: 1998, X-ray coronal changes during Halo CMEs. *Geophys. Res. Lett.* **25**, 2481. DOI. ADS.

Kashyap, V., Drake, J.J.: 1998, Markov-Chain Monte Carlo reconstruction of emission measure distributions: application to solar extreme-ultraviolet spectra. *Astrophys. J.* **503**, 450. DOI. ADS.

Krista, L.D., Reinard, A.: 2013, Study of the recurring dimming region detected at AR 11305 using the Coronal Dimming Tracker (CoDiT). *Astrophys. J.* **762**, 91. DOI. ADS.

Lemen, J.R., Title, A.M., Akin, D.J., Boerner, P.F., Chou, C., Drake, J.F., Duncan, D.W., Edwards, C.G., Friedlaender, F.M., Heyman, G.F., Hurlburt, N.E., Katz, N.L., Kushner, G.D., Levay, M., Lindgren, R.W., Mathur, D.P., McFeaters, E.L., Mitchell, S., Rehse, R.A., Schrijver, C.J., Springer, L.A., Stern, R.A., Tarbell, T.D., Wuelser, J.-P., Wolfson, C.J., Yanari, C., Bookbinder, J.A., Cheimets, P.N., Caldwell, D., Deluca, E.E., Gates, R., Golub, L., Park, S., Podgorski, W.A., Bush, R.I., Scherrer, P.H., Gummin, M.A., Smith, P., Auker, G., Jerram, P., Pool, P., Soufli, R., Windt, D.L., Beardsley, S., Clapp, M., Lang, J., Waltham, N.: 2012, The Atmospheric Imaging Assembly (AIA) on the Solar Dynamics Observatory (SDO). *Solar Phys.* **275**, 17. DOI. ADS.

Mason, J.P., Woods, T.N., Caspi, A., Thompson, B.J., Hock, R.A.: 2014, Mechanisms and observations of coronal dimming for the 2010 August 7 event. *Astrophys. J.* **789**, 61. DOI. ADS.

Munro, R.H., Gosling, J.T., Hildner, E., MacQueen, R.M., Poland, A.I., Ross, C.L.: 1979, The association of coronal mass ejection transients with other forms of solar activity. *Solar Phys.* **61**, 201. DOI. ADS.

Nuevo, F.A., Vásquez, A.M., Landi, E., Frazin, R.: 2015, Multimodal differential emission measure in the solar corona. *Astrophys. J.* **811**, 128. DOI. ADS.

Plowman, J., Kankelborg, C., Martens, P.: 2013, Fast differential emission measure inversion of solar coronal data. *Astrophys. J.* **771**, 2. DOI. ADS.

Reinard, A.A., Biesecker, D.A.: 2008, Coronal mass ejection-associated coronal dimmings. *Astrophys. J.* **674**, 576. DOI. ADS.

Robbrecht, E., Wang, Y.-M.: 2010, The temperature-dependent nature of coronal dimmings. *Astrophys. J. Lett.* **720**, L88. DOI. ADS.

Rust, D.M., Hildner, E.: 1976, Expansion of an X-ray coronal arch into the outer corona. *Solar Phys.* **48**, 381. DOI. ADS.

Sterling, A.C., Hudson, H.S.: 1997, Yohkoh SXT observations of X-ray "dimming" associated with a halo coronal mass ejection. *Astrophys. J. Lett.* **491**, L55. DOI. ADS.

Thernisien, A., Vourlidas, A., Howard, R.A.: 2009, Forward modeling of coronal mass ejections using STEREO/SECCHI data. *Solar Phys.* **256**, 111. DOI. ADS.

Thompson, B.J., Plunkett, S.P., Gurman, J.B., Newmark, J.S., St. Cyr, O.C., Michels, D.J.: 1998, SOHO/EIT observations of an Earth-directed coronal mass ejection on May 12, 1997. *Geophys. Res. Lett.* **25**, 2465. DOI. ADS.

Thompson, B.J., Cliver, E.W., Nitta, N., Delannée, C., Delaboudinière, J.-P.: 2000, Coronal dimmings and energetic CMEs in April – May 1998. *Geophys. Res. Lett.* **27**, 1431. DOI. ADS.

Tian, H., McIntosh, S.W., Xia, L., He, J., Wang, X.: 2012, What can we learn about solar coronal mass ejections, coronal dimmings, and extreme-ultraviolet jets through spectroscopic observations? *Astrophys. J.* **748**, 106. DOI. ADS.

Vásquez, A.M.: 2016, Seeing the solar corona in three dimensions. *Adv. Space Res.* **57**, 1286. DOI. ADS.

Vourlidas, A., Howard, R.A.: 2006, The proper treatment of coronal mass ejection brightness: a new methodology and implications for observations. *Astrophys. J.* **642**, 1216. DOI. ADS.

Vourlidas, A., Syntelis, P., Tsinganos, K.: 2012, Uncovering the birth of a coronal mass ejection from two-viewpoint SECCHI observations. *Solar Phys.* **280**, 509. DOI. ADS.

Vourlidas, A., Subramanian, P., Dere, K.P., Howard, R.A.: 2000, Large-angle spectrometric coronagraph measurements of the energetics of coronal mass ejections. *Astrophys. J.* **534**, 456. DOI. ADS.

Vourlidas, A., Howard, R.A., Esfandiari, E., Patsourakos, S., Yashiro, S., Michalek, G.: 2010, Comprehensive analysis of coronal mass ejection mass and energy properties over a full solar cycle. *Astrophys. J.* **722**, 1522. DOI. ADS.

Watanabe, K., Masuda, S., Segawa, T.: 2012, Hinode flare catalogue. *Solar Phys.* **279**, 317. DOI. ADS.

Wuelser, J.-P., Lemen, J.R., Tarbell, T.D., Wolfson, C.J., Cannon, J.C., Carpenter, B.A., Duncan, D.W., Gradwohl, G.S., Meyer, S.B., Moore, A.S., Navarro, R.L., Pearson, J.D., Rossi, G.R., Springer, L.A., Howard, R.A., Moses, J.D., Newmark, J.S., Delaboudiniere, J.-P., Artzner, G.E., Auchere, F., Bougnet, M., Bouyries, P., Bridou, F., Clotaire, J.-Y., Colas, G., Delmotte, F., Jerome, A., Lamare, M., Mercier, R., Mullot, M., Ravet, M.-F., Song, X., Bothmer, V., Deutsch, W.: 2004, EUVI: the STEREO-SECCHI extreme ultraviolet imager. In: Fineschi, S., Gummin, M.A. (eds.) *Telescopes and Instrumentation for Solar Astrophysics*, *Proc. SPIE* **5171**, 111. DOI. ADS.

Zarro, D.M., Sterling, A.C., Thompson, B.J., Hudson, H.S., Nitta, N.: 1999, SOHO EIT observations of extreme-ultraviolet "dimming" associated with a halo coronal mass ejection. *Astrophys. J. Lett.* **520**, L139. DOI. ADS.

Zhang, J., Dere, K.P., Howard, R.A., Vourlidas, A.: 2004, A study of the kinematic evolution of coronal mass ejections. *Astrophys. J.* **604**, 420. DOI. ADS.

Zhukov, A.N., Auchère, F.: 2004, On the nature of EIT waves, EUV dimmings and their link to CMEs. *Astron. Astrophys.* **427**, 705. DOI. ADS.